UC Davis

UC Davis Previously Published Works

Title

Large-Eddy Simulations of cavitation in a square surface cavity

Permalink

https://escholarship.org/uc/item/5vp3q3zm

Journal

Applied Mathematical Modelling, 38(23)

ISSN

0307-904X

Authors

Dai, S

Younis, BA

Sun, L

Publication Date

2014-12-01

DOI

10.1016/j.apm.2014.04.059

Peer reviewed

eScholarship.org Powered by the California Digital Library
University of California

Applied Mathematical Modelling 38 (2014) 5665–5683

Contents lists available at ScienceDirect

Applied Mathematical Modelling

journal homepage: www.elsevier.com/locate/apm

Large-Eddy Simulations of cavitation in a square surface cavity

Shaoshi Dai [a,*], Bassam A. Younis [b], Liping Sun [a]

[a] Deepwater Engineering Research Center, Harbin Engineering University, 150001, China
[b] Department of Civil and Environmental Engineering, University of California, Davis, CA 95616, USA

ARTICLE INFO

Article history:
Received 18 July 2013
Received in revised form 18 March 2014
Accepted 29 April 2014
Available online 9 May 2014

Keywords:
Cavitation
LES
Multiphase
Vortex shedding

ABSTRACT

We report on the development and application of a multiphase approach to the prediction of cavitation induced by high-speed flow over and within a square surface cavity. The approach entails employing a full cavitation model in conjunction with Large-Eddy Simulations in order to capture the initiation and development of bubble formations in turbulent-flow conditions. The incipient formation of the bubble cloud, and the flow processes of vortex shedding and shear-layer oscillations are tracked using the Volume of Fluid method. The validity of the computational approach was assessed by comparisons with experiments on cavitating flow over a hydrofoil. Application to the case of flow over and within a two-dimensional square cavity with cavitation clearly reveal the presence of traveling cavitation at the corner of the cavity trailing edge, and vortex cavitation within the cavity. It is shown that the collapse of cavitation bubbles results in an impact frequency that is higher than the frequency of the shear-layer oscillations. This implies that structural damage due to cavitation is likely to be most severe at the corner formed at the intersection of the cavity's trailing edge and the flat surface upstream of it.

© 2014 Elsevier Inc. All rights reserved.

1. Introduction

Cavitation, by which it is meant the formation and subsequent collapse of air bubbles in a moving fluid due to drop in the local pressure to below the vapor pressure, is known to occur in many areas of engineering practice such as on the surfaces of maneuvering underwater vehicles and on their rotating propellers, in water-supply systems generally and in pumps in particular, and in various components of other hydraulic machinery. In most cases, the collapse of the air bubbles upon contact with a solid surface imparts a significant transient load on the surface. This load can exceed by a significant margin the static design load thereby promoting structural failure by fatigue and excessive pitting, or the degradation of the overall performance of the system by the generation of vibrations and noise. The ability to accurately predict the occurrence and consequences of cavitation is therefore prerequisite to the safe and efficient design of systems where this phenomenon is likely to occur. The primary objective of this paper is to advance a computational approach that can be relied upon to meet this need.

The choice of a computational approach to the prediction of cavitation depends to a large extent on the mechanism underlying the initiation of local boiling, and this in turn depends on the geometry leading to reduction of the local pressure to a value below the vapor pressure. In this work, we are concerned with cavitation that occurs within a square surface cavity below a fast-moving stream. In certain conditions of flow Reynolds number and cavity aspect ratio, the shear layer that

* Corresponding author. Tel.: +86 (530) 312 8373; fax: +86 (530) 752 7872.
E-mail address: daishaoshi@163.com (S. Dai).

http://dx.doi.org/10.1016/j.apm.2014.04.059
0307-904X/© 2014 Elsevier Inc. All rights reserved.

Nomenclature

A	symbol representing $\rho\tau_{ij}$
B	viscous stress tensor, $\mathbf{B} = 2\tilde{\mu}S$
C	hydrofoil chord length
Cp	static pressure coefficient
C_p'	fluctuating pressure coefficient
C_w, C_s	constant coefficients
f_s, f_v, f_b	frequency of shear layer oscillation, vortex shedding and bubble movement respectively
F_c, F_e	vapor volume gasification and condensation coefficient
g_{ij}	velocity gradient tensor
L	characteristic scale of structure
m	mass of n-bubbles per unit volume
m_b	mass of bubble
n_b	number of bubbles per unit volume of mixture flow
$\dot{m}$	mass flow rate of net vapor
$\dot{m}_e^+$	vapor generation rate
$\dot{m}_e^-$	vapor condensation rate
p	absolute pressure
p_v	liquid vapor pressure
p_∞	reference pressure
R_b	bubble radius
Re	Reynolds number
S	rate of strain tensor
St	Strouhal number
t	moving time
u_i	Cartesian velocity
u_∞	reference velocity
V_B	volume of bubble
V_v	vapor volume
X	distance from monitoring points to corner point of leading edge

Greek symbols

α	angle of attack
α_v	vapor volume fraction
α_{nuc}	nuclei volume fraction
δ_{ij}	Kronecker delta
Δ	sub-grid characteristic length scale
μ_v, μ_l, $\tilde{\mu}$	dynamic viscosity of vapor, net liquid and mixture flow respectively
v	kinematic viscosity
v_{SGS}	sub-grid scale (eddy) viscosity
$\tilde{\rho}$, ρ_l, ρ_v	density of mixture, liquid density and vapor density respectively
σ	cavitation number
τ_{ij}	sub-grid stress tensor
Ω_{ij}	rotational stress tensor

Subscripts

i, j	Cartesian tensor indices
l	liquid phase
v	vapor phase

emerges from the upstream corner of the cavity becomes unstable and begins to oscillate at a discrete frequency associate with the shedding of vortices from that corner. The resulting reduction in pressure due to the vertical motion can be sufficiently large so as to cause cavitation to occur. The unsteady character of the flow, together with the fact that the flow is both multiphase and turbulent, poses this problem of shear-layer induced cavitation as a severe challenge to both experimentation and to computational modeling. In recent years, considerable efforts have been expended in both of these areas [1–8]. In connection with computational modeling, it is now generally accepted that predictions based on potential-flow theory are no longer adequate for the purpose of engineering design. It is also generally accepted that the accurate representation of this phenomenon requires the solution of the full set of the Navier–Stokes equations at high Reynolds number. Since Direct

Numerical Simulations (DNS) that require resolution of the small-scale turbulent motions are not currently feasible due to computer limitations, it is customary to time-average these equations and to then deal with the resulting unknown Reynolds stresses via a suitable turbulence model. A review of the published literature indicates that the most widely used turbulence model in this application is the k-ε, two-equation, eddy-viscosity closure. Previous studies utilizing this model include those of Huang et al. [1], Li et al. [2], Barre et al. [3] and Coutier-Delgosha et al. [4] who used this model for the prediction of cavitation in a wide variety of conditions. In many cases, it was found necessary to modify the standard k–ε model in some way to bring about closer agreement with the experimental data. This element of empiricism has led some researchers to consider the use of more advanced turbulence models to predict cavitation [5,6], but a generally-applicable model has not emerged so far.

The alternative to DNS and to turbulence modeling is to use Large-Eddy Simulations (LES) to resolve the large-scale structures while taking into account the effects of the small-scale motions via a suitable model. Regarding the cavitation in an open cavity, Shams et al. [7] reported on predictions of cavitation of the trailing edge using LES, but no details were provided on the bubble-vortex coupling at the shear layer, or on the effects of the local void faction. The prediction of these two parameters constitutes the main focus of the present study. Moreover, a number of computational issues remained to be resolved in this particular flow [8], and some of these will be addressed here. The principal difference between the present and the previous work is thus in the use of LES in preference to eddy-viscosity closures, and to fully account for the effects of turbulence on the bubble-water interactions. While LES does not by itself provide solutions that are free of modeling errors (something that can only be achieved by DNS), it is expected that these errors will be more limited in severity and extent with advances in computer capabilities. Meanwhile, it is expected that the increased numerical resolution necessitated by the need to resolve the unsteady small-scale motions in LES will also lead to better tracking of the air bubbles that are formed by cavitation. This will be demonstrated in subsequent sections of this paper.

2. Mathematical formulation

The present computational model consists of three distinct but coupled components: a finite-volume method for solving the equations that govern the conservation of mass and momentum in the Large-Eddy Simulations framework, a cavitation model to capture the formation of air bubbles, and a multi-phase model to handle the interactions between the air bubbles and the water flow field. These models are now presented in turn.

2.1. Conservation equations and the LES model

By assuming thermodynamic equilibrium of the gas–liquid phases, the Continuity equation and the Navier–Stokes equations for variable-density flows are given as:

$$\frac{\partial\tilde{\rho}}{\partial t}+\frac{\partial}{\partial x_j}(\tilde{\rho}u_j)=0, \tag{1}$$

$$\frac{\partial(\tilde{\rho}u_i)}{\partial t}+\frac{\partial}{\partial x_j}(\tilde{\rho}u_iu_j)=-\frac{\partial p}{\partial x_i}+\frac{\partial}{\partial x_j}(2\tilde{\mu}S)+f, \tag{2}$$

where $\sim$ represents volume-weighted quantity i.e.

$$\tilde{\rho}=\alpha_v\rho_v+(1-\alpha_v)\rho_l.$$

$$\tilde{\mu}=\alpha_v\mu_v+(1-\alpha_v)\mu_l$$

and a_v is the vapor volume fraction, which is obtained by solving the transport equation presented below. The quantity $S=\frac{1}{2}(\nabla u+\nabla u^T)$ is the rate of strain tensor, u_i is the velocity, ρ_l and ρ_v are density of net liquid and vapor, μ_l and μ_v are the dynamic viscous coefficients of net liquid and vapor, p the pressure, f is the gravity.

By application of a Gaussian filter to Eqs. (1) and (2) and by taking the volume average we obtain:

$$\frac{\partial(\tilde{\rho}\bar{u}_i)}{\partial t}+\frac{\partial}{\partial x_j}(\tilde{\rho}\bar{u}_i\bar{u}_j)=-\frac{\partial\bar{p}}{\partial x_i}+\frac{\partial}{\partial x_j}(B-A)+f, \tag{3}$$

where $\mathbf{B}=2\tilde{\mu}S$ is viscous stress tensor. $\mathbf{A}=\tilde{\rho}\tau_{ij}$ and $\tau_{ij}=\overline{u_iu_j}-\bar{u}_i\bar{u}_j$ is the subgrid stress tensor.

The Sub-Grid Scale (SGS) model needed to approximate the values of τ_{ij} is based on the Smagorinsky assumption of a linear stress–strain relationship, that is:

$$\tau_{ij}=-2\upsilon_{SGS}\bar{S}_{ij}+\frac{1}{3}\tau_{kk}\delta_{ij}, \tag{4}$$

$$\upsilon_{SGS}=(C_s\Delta)^2|\bar{S}|, \tag{5}$$

where δ_{ij} is the Kronecker delta, υ_{SGS} is the eddy viscosity and $\bar{S}_{ij}$ is the strain rate tensor for the resolved scale, $\bar{S}_{ij}=\frac{1}{2}\left(\frac{\partial\bar{u}_i}{\partial x_j}+\frac{\partial\bar{u}_j}{\partial x_i}\right)$. C_s is the Smagorinsky coefficient, Δ is the subgrid characteristic length scale, and $|\bar{S}|=\sqrt{2\bar{S}_{ij}\bar{S}_{ij}}$.

This model does not perform well in a number of situations, including the one of present interest. Thus, for example, the rotational effects associated with the large-scale separation are not adequately accounted for. Also, the viscous coefficient is not zero very close to the wall although the turbulence activity there is very weak. Moreover, in more complex geometries, there is considerable ambiguity in how to interpret the SGS model in relation to the numerical grid used for the computations. It is for these reasons that the conventional SGS model was abandoned in this study in favor of an alternative model proposed by Nicond and Ducros [9] which takes into account the influence of the ratio of strain and rotation. In this model, it is generally preferable to consider the traceless symmetric part of the square of the velocity gradient tensor which is given as:

$$S_{ij}^d = \frac{1}{2}\left(\bar{g}_{ij}^2 + \bar{g}_{ji}^2\right) - \frac{1}{3}\delta_{ij}\bar{g}_{kk}^2, \tag{6}$$

where $\bar{g}_{ij}^2 = \bar{g}_{ik}\bar{g}_{kj}$.

The anti-symmetric part of $\bar{g}$ is written as:

$$\Omega_{ij} = \frac{1}{2}\left(\frac{\partial \bar{u}_i}{\partial x_j} - \frac{\partial \bar{u}_j}{\partial x_i}\right). \tag{7}$$

The tensor defined by Eq. (6) can be rewritten in terms of $\bar{S}$ and $\bar{\Omega}$:

$$S_{ij}^d = \bar{S}_{ik}\bar{S}_{kj} + \bar{\Omega}_{ik}\bar{\Omega}_{kj} - \frac{1}{3}\delta_{ij}\left[\bar{S}_{mn}\bar{S}_{mn} - \bar{\Omega}_{mn}\bar{\Omega}_{mn}\right]. \tag{8}$$

According to the Cayley–Hamilton theorem, the quantity $S_{ij}^d S_{ij}^d$ can be written as:

$$S_{ij}^d S_{ij}^d = \frac{1}{6}(S^2S^2 + \Omega^2\Omega^2) + \frac{2}{3}S^2\Omega^2 + 2IV_{S\Omega}, \tag{9}$$

where $S^2 = \bar{S}_{ij}\bar{S}_{ij},\ \Omega^2 = \bar{\Omega}_{ij}\bar{\Omega}_{ij},\ IV_{S\Omega} = \bar{S}_{ik}\bar{S}_{kj}\bar{\Omega}_{jl}\bar{\Omega}_{li}$.

Depending on the value of $S_{ij}^d S_{ij}^d$, the turbulence structures can be associated with either high strain rates, high rotation rates, or both. Thus defining a spatial operator $\overline{OP}$ to replace $\overline{|S|}$, $\overline{OP}$ will behave like y^3 near a wall, at the same time by scaling it must be of $O(1)$ near a wall before it being used in the subgrid scale model formulation (Eq. (4)). This has the effect of eliminating the numerical instabilities that can arise in the computations. Note that $\overline{OP}$ is proportional to $\overline{OP_1} = (S_{ij}^d S_{ij}^d)^{3/2}$ and is inversely proportional to $\overline{OP_2} == (\bar{S}_{ij}\bar{S}_{ij})^{5/2} + (S_{ij}^d S_{ij}^d)^{5/4}$.

The revised model is now given as:

$$\upsilon_{SGS} = (C_w\Delta)^2\frac{\overline{OP_1}}{\overline{OP_2}} = (C_w\Delta)^2\frac{(S_{ij}^d S_{ij}^d)^{3/2}}{(\bar{S}_{ij}\bar{S}_{ij})^{5/2} + (S_{ij}^d S_{ij}^d)^{5/4}},$$

where $C_w = C_s^2\frac{\langle\sqrt{2}(\bar{S}_{ij}\bar{S}_{ij})^{3/2}\rangle}{\langle\bar{S}_{ij}\bar{S}_{ij}\overline{OP_1}/\overline{OP_2}\rangle},\ C_s = 0.18$

C_w is a constant usually assigned a value in the range $0.55 \leqslant C_w \leqslant 0.6$. Comte-Bellot et al. [10] obtained good results by taking $C_w = 0.5$. This value will be used in the present study.

2.2. Multiphase flow model

For the prediction of cavitation in the open cavity, we adopt a model for mixed and homogeneous single flow where the mixture density depends on an equilibrium transport equation for the gas–liquid phases. Thus Eqs. (1) and (3) for conservation of mass and momentum are supplemented by an equation for the gas volume fraction:

$$\frac{\partial}{\partial t}((1-\alpha_v)\rho_l) + \frac{\partial}{\partial x_j}((1-\alpha_v)\rho_l u_j) = -\dot{m}, \tag{10}$$

where $\dot{m}$ is the net rate of change of vapor content which is calculated by using the phase transition models. Combining Eqs. (1) and (10) yields a relation between the mixture density and vapor volume fraction.

2.3. Phase transition model

The cavitation model used in this study is based on Rayleigh–Plesset Equation (RPE) which describes the generation and collapse of bubble to estimate the rate of vapor production. The dynamic growth of the bubble can be described by RPE as follows:

$$R_b\ddot{R}_b + \frac{3}{2}\dot{R}_b^2 + \frac{2\sigma}{\rho_l R_b} + \frac{4v_l}{R_b}\dot{R}_b = \frac{p_v - p}{\rho_l}, \tag{11}$$

where $\dot{R}_b = \frac{dR_b}{dt}$, R_b is the radius of bubble, p_v the vapor pressure in the bubble, p is pressure in the surrounding liquid and ρ_l is liquid density.

In this work, the following two assumptions were made: (i) the growth and collapse of bubbles follow the RPE neglecting higher order terms, viscous terms and the effects of surface tension. This is due to the fact that the acceleration is only necessary in the initial birth stage of cavitation and it can be neglected in other cases [11], and (ii) there are no thermal barriers to bubble growth:

$$\text{Based on these assumptions, the velocity of bubble radius is given by : } \frac{dR_b}{dt} = \left(\frac{2}{3}\frac{p_v - p}{\rho_l}\right)^{\frac{1}{2}}. \tag{12}$$

Based on the volume change of a single bubble, mass changing rate is given by: $\frac{dm_b}{dt} = 4\pi\rho_v R_b^2 \frac{dR_b}{dt}$.

If the number of bubbles per unit volume of mixture is n_b, then the volume fraction of vapor becomes: $\alpha_v = n_b \frac{4}{3}\pi R_b^3$. Moreover, the mass transfer rate of n-bubbles per unit volume is:

$$\frac{dm}{dt} = n_b \rho_v \frac{dV_B}{dt} = 4\pi n_b \rho_v R_b^2 \frac{dR_b}{dt}. \tag{13}$$

The mass transfer rate can be derived based on vapor volume fraction:

$$\dot{m} = \frac{3\alpha_v \rho_v}{R_b}\frac{dR_b}{dt}. \tag{14}$$

The mass transfer rate has two parts. One is source terms ($\dot{m}_e^+$) representing the vapor generation during cavitation, the other is sink terms ($\dot{m}_e^-$) accounting for possible condensation rate. Using Kubota model [12] the mass transfer rate is:

$$\begin{aligned} \dot{m}_e^+ &= F_c \bullet \frac{3\alpha_{nuc}(1-\alpha_v)\rho_v}{R_b}\sqrt{\frac{2}{3}\frac{|p_v - p|}{\rho_l}}\mathrm{sgn}(p_v - p) \quad p \leqslant p_v, \\ \dot{m}_c^- &= F_e \bullet \frac{3\alpha_{nuc}(1-\alpha_v)\rho_v}{R_b}\sqrt{\frac{2}{3}\frac{|p_v - p|}{\rho_l}}\mathrm{sgn}(p_v - p) \quad p > p_v. \end{aligned} \tag{15}$$

In the above, the radius for cavitation bubble R_b is replaced by R_{nuc}, namely $R_{nuc} = 1$ μm. a_{nuc} is the vapor volume fraction for the nuclei ($a_{nuc} = 5 \times 10^{-4}$). The vapor volume gasification coefficients were assigned the values $F_c = 50$ and $F_e = 0.01$ based on the experimental data of Shen and Dimotaks [13] and Gerber [14].

The final model thus consists of substituting Eq. (15) into Eq. (10) and then by simultaneously solving Eqs. (1), (3) and (10).

In order to track the transient liquid–gas interface, we use the Volume of Fluid (VOF) method wherein the tracking of the interface between two phases is accomplished by solving the continuity equation for the volume fraction of the two phases i.e. the water and the vapor in this case. The vapor volume fraction α_v is determined by the continuity equation (10). A fully implicit scheme is used for the time discretization, and the transport equation is solved iteratively for each of the secondary-phase volume fractions at each time step.

3. Verification of the computational model

The equations presented in Section 2 were solved using a three-dimensional finite-volume solver. Discretization of the convective terms was by second-order accurate central differencing. This is the customary practice in most cases where Large-Eddy Simulations are involved. Temporal discretization was also second-order accurate utilizing a multi-step scheme. Concerning the numerical accuracy of the simulations, this is a controversial issue in LES since by refining the grid, the model for the Sub-Grid Scale motions is also changed since the characteristic sub-grid length-scale is taken simply to be the cubic root of the cell volume. In principle, therefore, truly grid-independent results can only be achieved when Large-Eddy Simulations become, in effect, Direct Numerical Simulations. Unlike the case with RANS, where a quantitative measure of grid dependence can be obtained using e.g. a method based on Richardson extrapolation, no such procedure is available for LES. We have therefore followed the usual practice of employing the finest grid that can be accommodated by the available computer platform and relied on the Sub-Grid Scale model to account for the effects of the motions that were too small to capture. Concerning the remaining computational details, the SIMPLE algorithm was used to calculate the pressure field by coupling the solution of the continuity and momentum equations. In performing the calculations where cavitation was expected to occur, the computations were first started in single-phase mode until convergence was achieved and then thereafter commencing the calculation of cavitation. In what follows, we verify the computational model's performance against the benchmark cases of cavitation from a submerged hydrofoil at incidence, and the flow-induced oscillations over an open cavity at high Reynolds number.

3.1. Cavitating flow over a hydrofoil

Cavitation in the flow over a submerged hydrofoil at incidence has been the subject of numerous computational and experimental studies [1–3]. In this work, we validate the model using the parameters of the Clark-y hydrofoil for which experimental data are available [15–17]. The Clark-y hydrofoil is the most typical planar-convex airfoil. This kind of hydrofoil has round head, linear lower chord and curvilinear upper chord. The hydrofoil is shown in Figs. 1 and 2 where the computational grid is also shown. The cavitation number (σ) is taken as 0.8, the angle of attack angle is 8°, and the Reynolds number (based on the chord length c and reference velocity) is 7.5×10^5. Following Wang et al. [15], the computation domain extended to a distance of 11.5 chord lengths in the streamwise direction with the inlet boundary being located at distance 2.5 chord lengths upstream of the leading edge. The outflow boundary was located at 8 chord lengths downstream of the trailing edge. In the other two directions, the computational domain extended to a distance of 3 chord lengths from the hydrofoil's center (see Fig. 1).

The computations were performed on a structured hexahedral mesh with a C-C topology being used around the hydrofoil to closely match the contours of the leading edge. The computational mesh consisted of 118,368 active cells (Figs. 1 and 2). The smallest grid size of the first layer adjacent to the wall was 10^{-6} m. The boundary conditions used for these computations were as follows: at inlet, a uniform velocity profile was prescribed corresponding to the experimental value of Reynolds number. At outlet, the pressure was fixed to the atmospheric value. At the upper, lower and side boundaries, slip conditions was applied. The no-slip condition was applied at the walls. The computational time step is set to be 10^{-4} s. Iterations were performed at each time step with the convergence criterion taken to be when the absolute sum of all residuals fell to a value below 10^{-4}. This level of convergence was typically achieved after 3 iterations.

Comparison between the predicted and measured cavitation cloud (presented in the form of the vapor volume fraction) is shown in Fig. 3. In that figure, t_0 is the initial time of cavitation. Also shown in Fig. 3 are the results of Huang [17] obtained using the RNG two-equation model of turbulence. The figure shows the time evolution of cavitation flow from the sheet cavitation stage to the cloud cavitation stage. It is clear that the shape of the cavitation cloud is well reproduced in the present predictions compared to both experimental findings and the previous calculations. Some differences between predictions and measurements are apparent. These must be viewed in the light of the difficulty in obtaining accurate measurements in a highly complex, unsteady flow in a confined space. A more quantitative assessment of the model's performance can be obtained by comparing the predicted and measured values of the lift and drag coefficients. This is done in Table 1 where it can be seen that the maximum differences between predictions and measurements are well within the bounds of

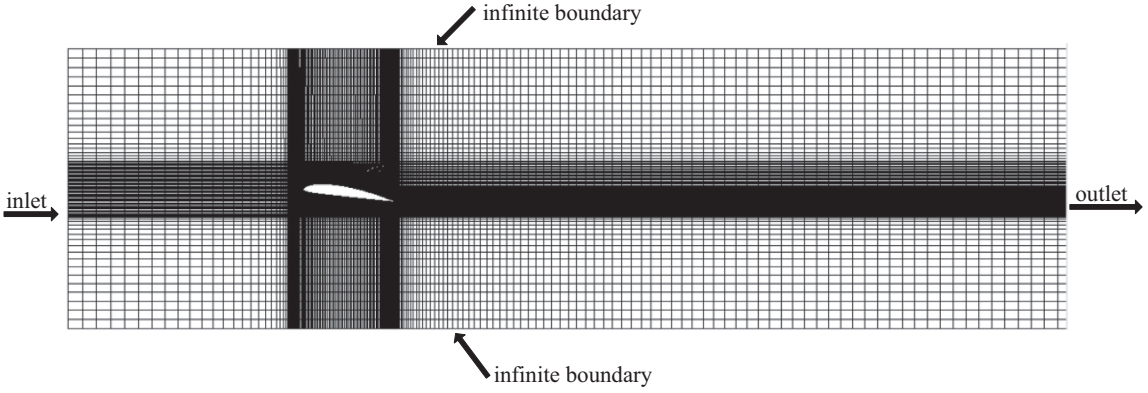

Fig. 1. Hydrofoil geometry and grid blocking arrangement.

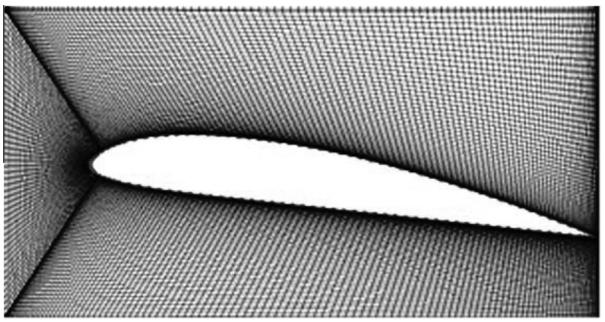

Fig. 2. Grid distribution near the hydrofoil.

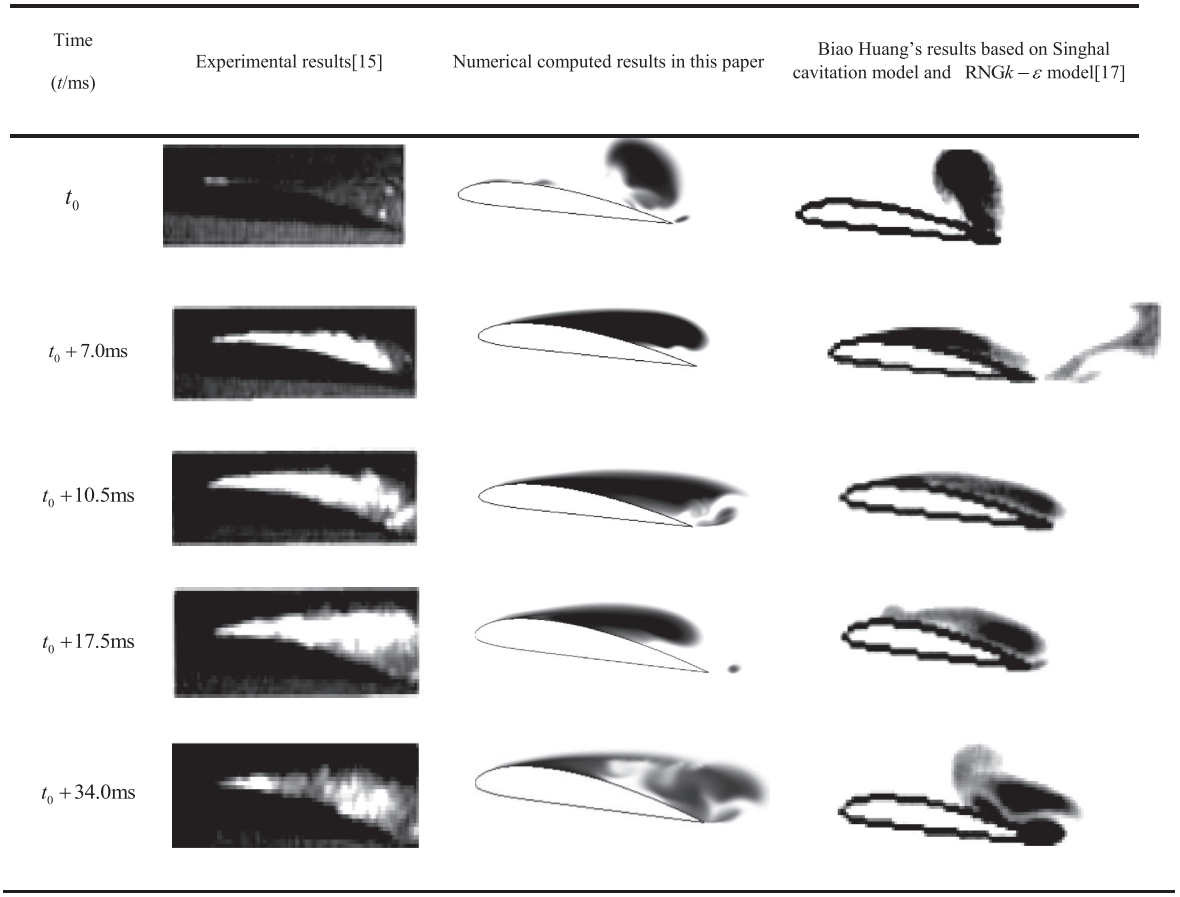

Fig. 3. Predicted and measured cavitation cloud for the Clark-y hydrofoil.

Table 1
Predicted and measured lift and drag coefficients for submerged hydrofoil.

$\sigma = 0.8$	Numerical calculated results base on LES method	Experimental results [15]	Calculated error (%)
C_l	0.730	0.770	5.2
C_d	0.123	0.115	7.8

experimental uncertainty. The time history of these parameters is presented in Fig. 4 where it can be seen that the fluctuations in these parameters are quite significant and fairly random.

3.2. Flow-induced oscillations in open cavity

This case concerns the flow-induced oscillations that occur inside an open cavity without cavitation (see Fig. 5 for geometry). The purpose of computing this flow is to validate the LES model that will subsequently be used for the case cavitation. The boundary conditions were as before: specified uniform velocity at inlet, and fixed pressure at outlet where the reference pressure was set to atmospheric. The computations were performed at Reynolds number (based on length of open-cavity in streamwise direction) of 2.06×10^5.

The computational grid is shown in Fig. 6. The computational domain extends to a distance of 5.7 cavity lengths in the streamwise direction, the inlet plane being at distance 1.7 lengths upstream of the leading edge and the outflow boundary at distance of 3.0 lengths from the trailing edge. The computational grid was formed in multi-blocks with hexahedral meshes that were non-uniformly distributed in order to better resolve the near-wall layer. In order to capture the vortex generation and development, the first layer mesh adjacent to the wall was placed close enough to the surface such that $y^+ < 1$. The dimension of the smallest mesh was 10^{-5} m and that of the largest mesh was 4×10^{-3} m. The total number of elements was 110,507.

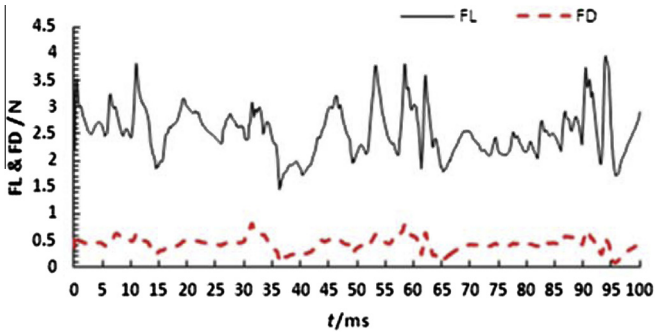

Fig. 4. Time series of lift and drag coefficients for hydrofoil with cavitation ($\sigma = 0.8,\ \alpha = 8^{\circ}$).

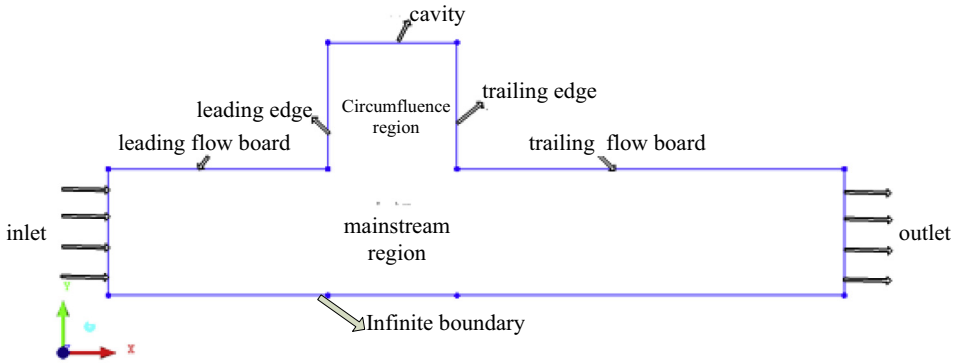

Fig. 5. Geometry of open surface cavity.

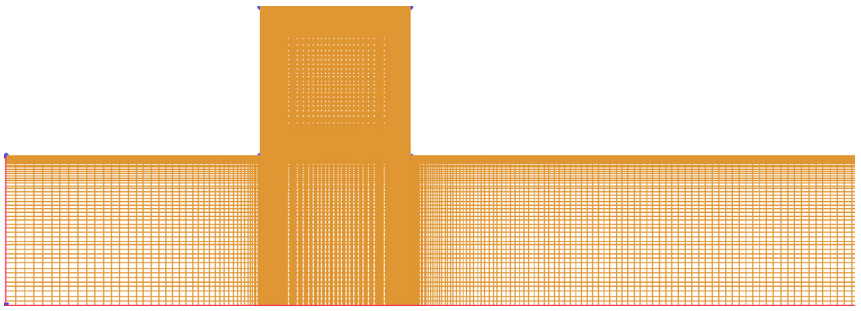

Fig. 6. Grid distribution for cavity flow.

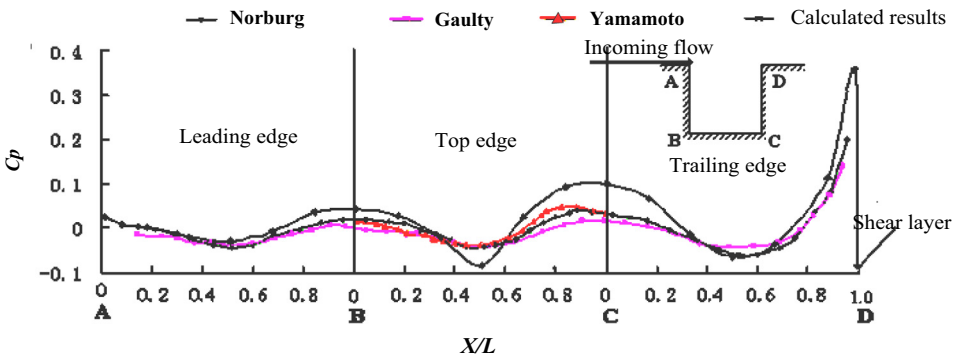

Fig. 7. Predicted and measured wall static pressure coefficient Cp ($\mathrm{Re} = 2.06 \times 10^{5}$).

Comparison between the predicted and measured wall static-pressure distribution is presented in Fig. 7. Also plotted there are results from the experimental studies of Yamamoto et al. [18] and Chang [19]. It can be seen that there is close agreement between the computations and measurements over a large portion of the cavity except, perhaps, very close to the corners where some underprediction is observed. At the horizontal surface of the cavity ($X/L \approx 0.9$), the wall static pressure attains its maximum value. At $X/L = 1.0$, at the upper corner of the trailing edge, the pressure is at its minimum. These results show that the minimum pressure value always appears at the corner of trailing edge without cavitation. A similar conclusion was also arrived at in [20].

4. Results and discussion

Attention is now turned to the central problem addressed here, namely that of flow over an open cavity in conditions leading to the occurrence of cavitation. The flow geometry is identical to that of the previous case (Fig. 5). In order to capture the small cavitation bubbles and the vortices that are expected to form inside the open cavity, a structured hexahedral grid was again adopted for this case where, as before, the grid was concentrated near the walls with the smallest grid size being equal to the expected radius of a bubble (10^{-6} m) while the largest size was equal to 3×10^{-3} m. Total number of elements was 170,257 (see Fig. 6). The time step was set equal to 10^{-4} s in order to capture the collapse of bubbles. The CPU time required for a typical run was about 96 h on a 32 bit computer with 2 Gb memory. In order to adequately analyze the flow, 24 observation points were located on the cavity walls (see Fig. 8). As before, the boundary conditions consisted of a specified uniform velocity at inlet and a fixed pressure at outlet. The remaining boundaries were designated as planes of symmetry. Further details are given in Table 2.

In this study, the relevant non-dimensional parameters are defined as follows:

$$\sigma = \frac{2(p_\infty - p_v)}{\rho_l u_\infty^2}, \quad \alpha_v = \frac{V_v}{V}, \quad Cp(x,y) = \frac{2(\overline{p}(x,y) - p_\infty)}{\rho_l u_\infty^2} \quad \text{and} \quad Cp'(x,y) = \frac{2\left(\sqrt{\sum [p(x,y,t) - \overline{p}(x,y,t)]^2 / N}\right)}{\rho_l u_\infty^2},$$

where σ is the cavitation number, α_v is vapor volume fraction, V_v is vapor volume, Cp is the mean wall static-pressure coefficient and C_p' is the fluctuating pressure coefficient, v is the kinetic viscosity coefficient, N is the number of samples used in

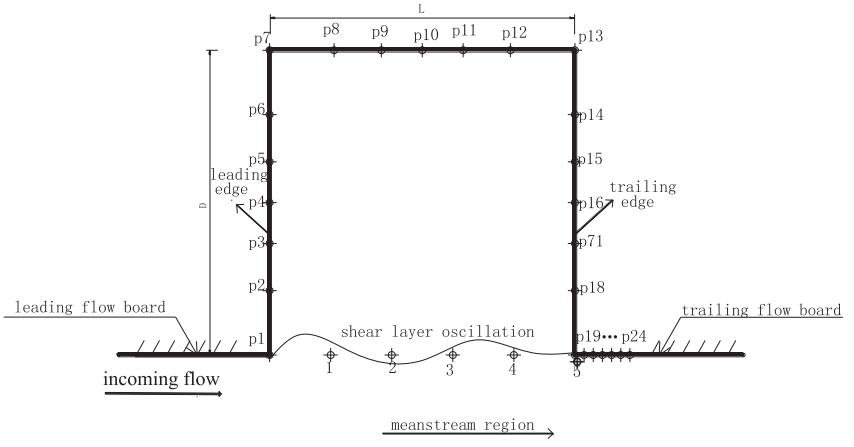

Fig. 8. Location of wall-pressure monitoring points.

Table 2
Boundary conditions and physical parameters.

Inlet boundary	$u = u_\infty$, $v = 0$, $w = 0$
Outlet boundary	$p = 36$ KPa + $\rho_l g h$
Cavity boundary	$u_n = 0$, $u_\tau = 0$
Infinite boundary	$u_\tau \neq 0$
Initial condition	$u = u_\infty$, $v = 0$, $w = 0$
	$T = 20\,^\circ$C; $\alpha_l = 1$
	$\rho_l = 998$ kg/m^3
	$\rho_v = 0.017$ kg/m^3
	$\alpha_l = 1$; $\alpha_v = 0$
Saturation vapor pressure	$p_v = 2300$ Pa
Cavitation number	$\sigma = 2.176, 1.615, 1.249, 0.996, 0.816$
Reynolds number	Re = 5.98×10^5–9.96×10^5, ΔRe = 1×10^5

the averaging process, p_∞ is the average steady pressure taken to be that of the inlet flow and $p(x,y,t)$ is the transient pressure at arbitrary position in flow region. p_v is the liquid vapor pressure. f is frequency, f_s, f_v and f_b represent frequency of shear layer oscillation, frequency of vortex shedding and of the bubble movement, respectively.

4.1. Traveling cavitation at corner of trailing edge

An overview of the results can be seen from Figs. 9 and 10 which show, respectively, the location of the vapor volume fraction and the velocity vectors inside the cavity. As expected, flow separation occurs from the sharp leading-edge corner leading to the formation of a layer of high shear. This layer is inherently unstable and it oscillated as vortices are shed from this corner. At the beginning, clear traveling cavitation is generated at the corner of trailing edge and at the shear layer. Generation of traveling cavitation is close to the shear layer oscillation. When the shear layer reaches the attachment region, it rises along the side of downstream wall. Above the attachment region, fluid is entrained into the inner cavity, while below the attachment region fluid flows into the free stream region. A high-pressure region appears near the attachment point as can be seen in Fig. 11, while a low-pressure region appears at the corner of trailing edge which is where the traveling cavitation bubbles are initially generated. A detailed time evolution of the vapor volume fraction showing the traveling cavitation bubble is shown in Fig. 11 where it can be seen that traveling cavitation appears at the corner of trailing edge which is where the minimum pressure is located. The process of generation and subsequent movement of traveling cavitation can be

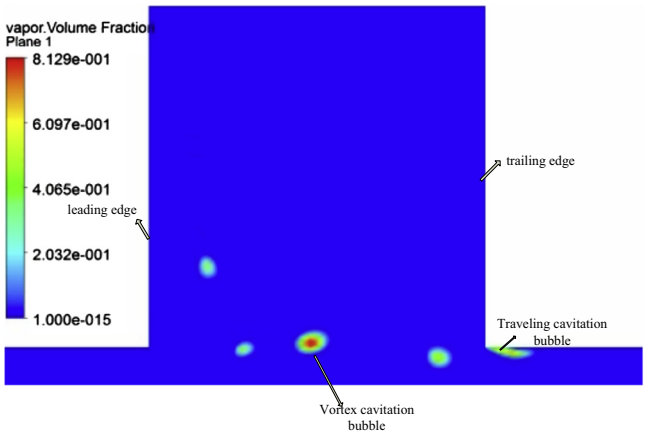

Fig. 9. Predicted vapor volume fraction in open cavity ($\sigma = 0.816,\ \mathrm{Re} = 9.96 \times 10^5,\ t = t_0 + 123.5$ ms).

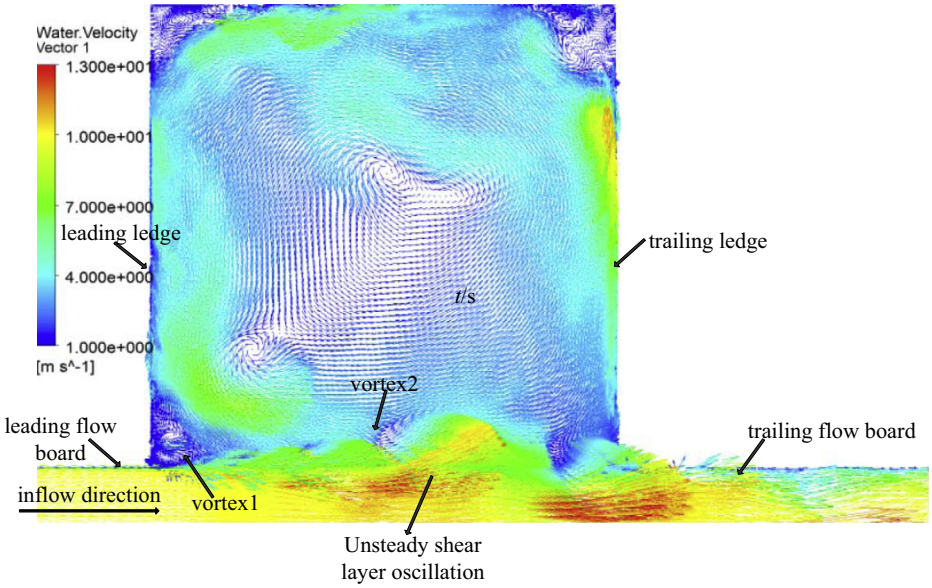

Fig. 10. Velocity vectors in open cavity ($\sigma = 0.816,\ \mathrm{Re} = 9.96 \times 10^5,\ t = t_0 + 123.5$ ms).

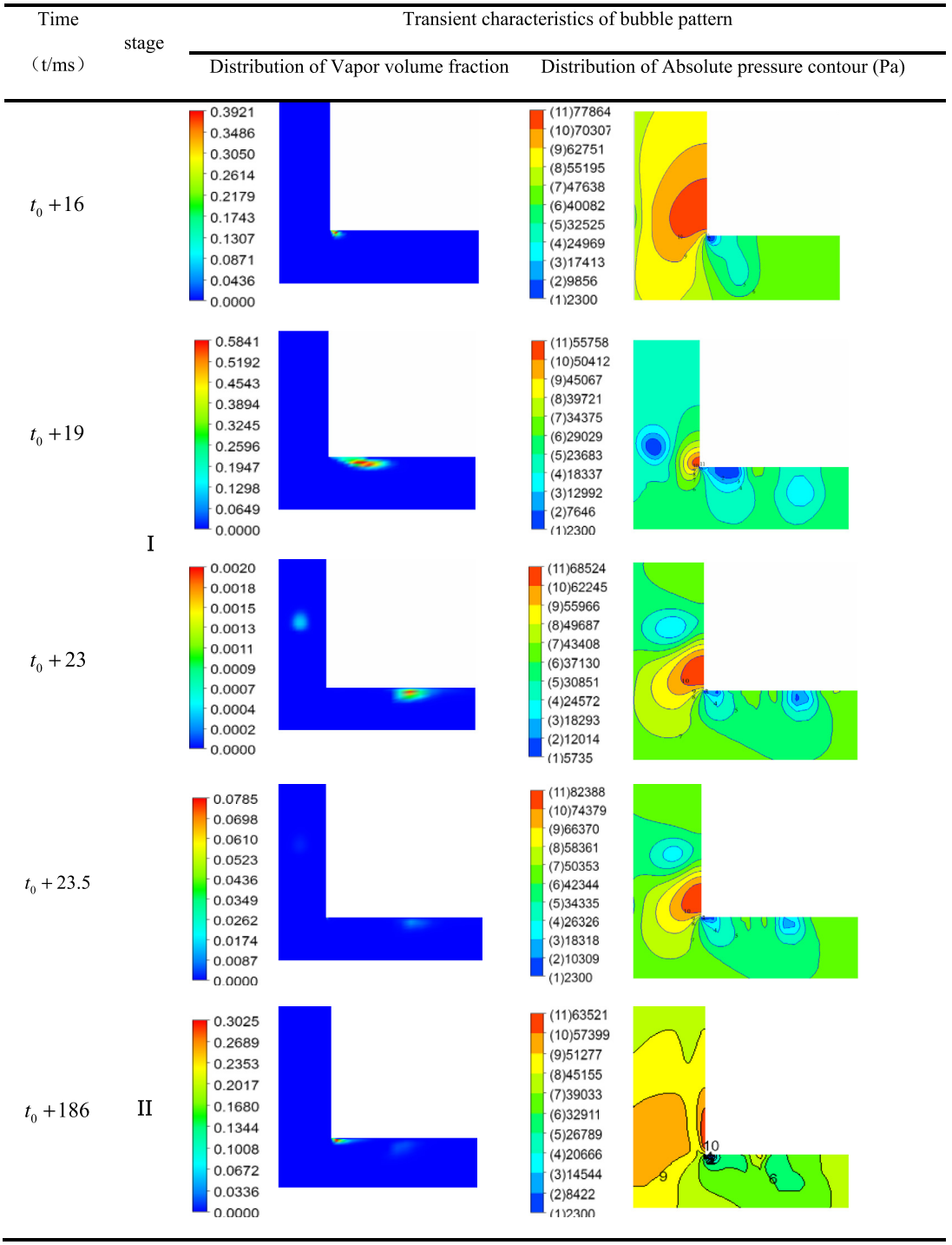

Fig. 11. Time evolution of traveling cavitation ($\sigma = 0.816,\ \mathrm{Re} = 9.96 \times 10^5$).

divided into two stages. The first stage is the inception and movement of a single traveling cavitation, while the second stage is the generation and movement of secondary traveling cavitation. We define the initial time of transient calculation as t_0, whole calculation time is t. At time $t = t_0 + 16$ ms, a single small cavitation bubble appears at the corner of the trailing edge which at time $t = t_0 + 19$ ms begins to grow with the expansion of the local low-pressure region. There are also changes to the bubble shape. A single bubble diffuses along the wall and moves downstream while being stretched because the minimum pressure point exists at larger adverse pressure gradient along the normal direction of the surface of trailing edge.

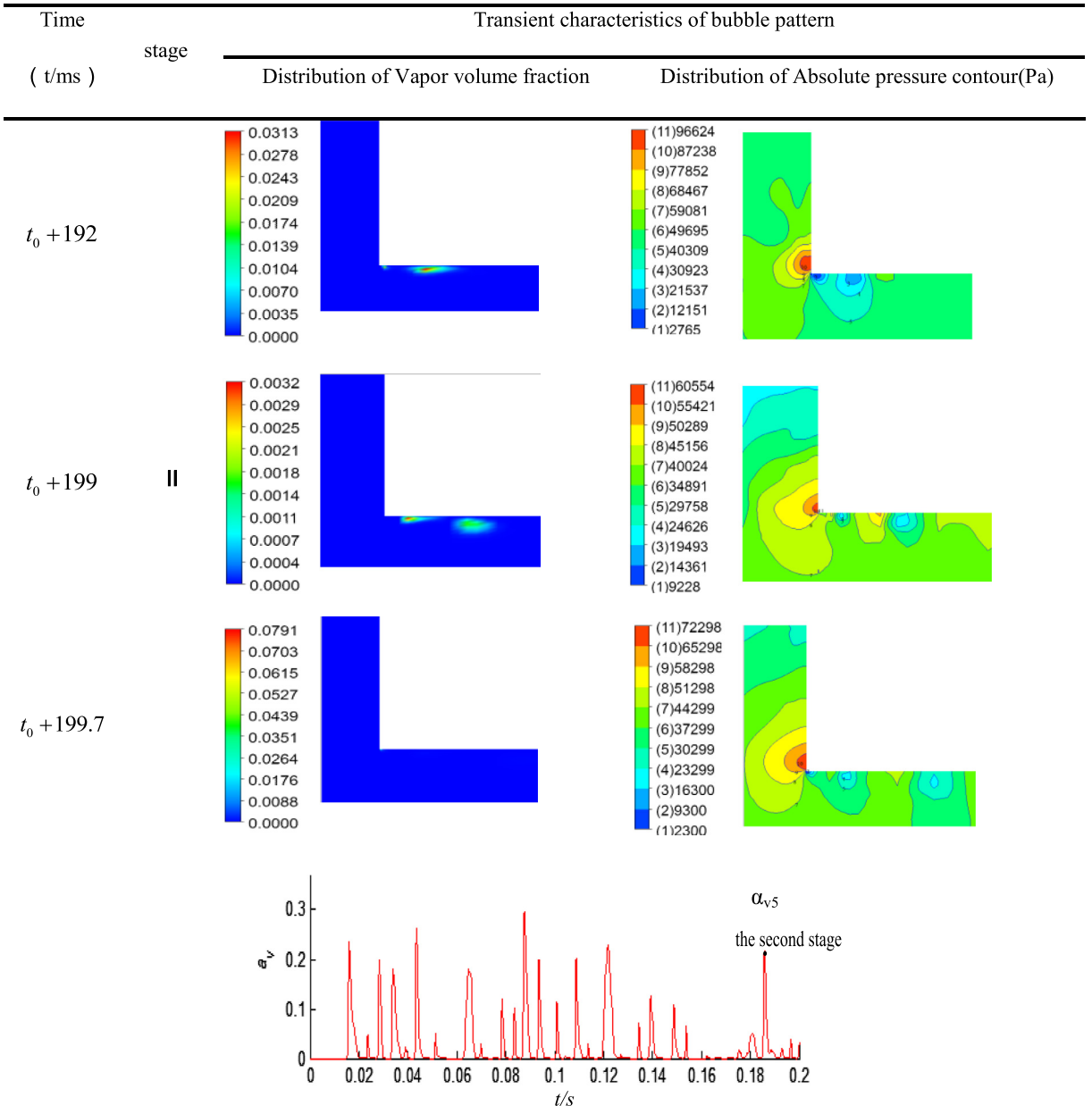

Fig. 11 (*continued*)

Thereafter, the bubble starts to contract and become smaller due to gradually increasing external pressure. Bubble collapses and disappears after 0.5 ms. In the second stages, a new cycle begins. At time $t_0 + 186$ ms, the first bubble appears then the second traveling cavitation generates at the corner of trailing edge after 5 ms. The two bubbles move downstream along the trailing-edge wall. At time $t = t_0 + 199$ ms, the second bubble begins to grow and stretch while the nucleus of the first bubble disappear and begin to contract. Due to increasing adverse pressure gradient, two bubbles collapse during motion. The generation, development and subsequent collapse of the traveling cavitation change periodically. Although the process of the second inception is the same as the first, the vapor volume fraction is a little lower, and its time duration is also small.

4.2. Vortex cavitation at shear layer

At the leading edge of the open cavity, an intense region of mixing is formed due to the presence of high shear generated below the moving stream. The free shear-layer is inherently unstable leading to the precession of high-intensity vortices.

Due to the sudden expansion of the flow area, the velocity within the inner cavity decreases while the pressure there is increased leading to the formation near the leading edge of a local region of adverse pressure gradients. As a result, irregular vortices are generated, as can be seen in Fig. 12. Due to advection by the incoming flow, the vortices enter the positive pressure gradient region and diffuse into the flow. After that the vortices are convected in the streamwise direction, accompanied by shear layer oscillation. When the pressure at the center of the vortex drops below the vapor pressure, vortex cavitation occurs.

The predicted time evolution of vortex cavitation and the distribution of absolute pressure are shown in Figs. 12 and 13 respectively. It is clear from these figures that the motion of the vortex cavitation is closely related to the pressure

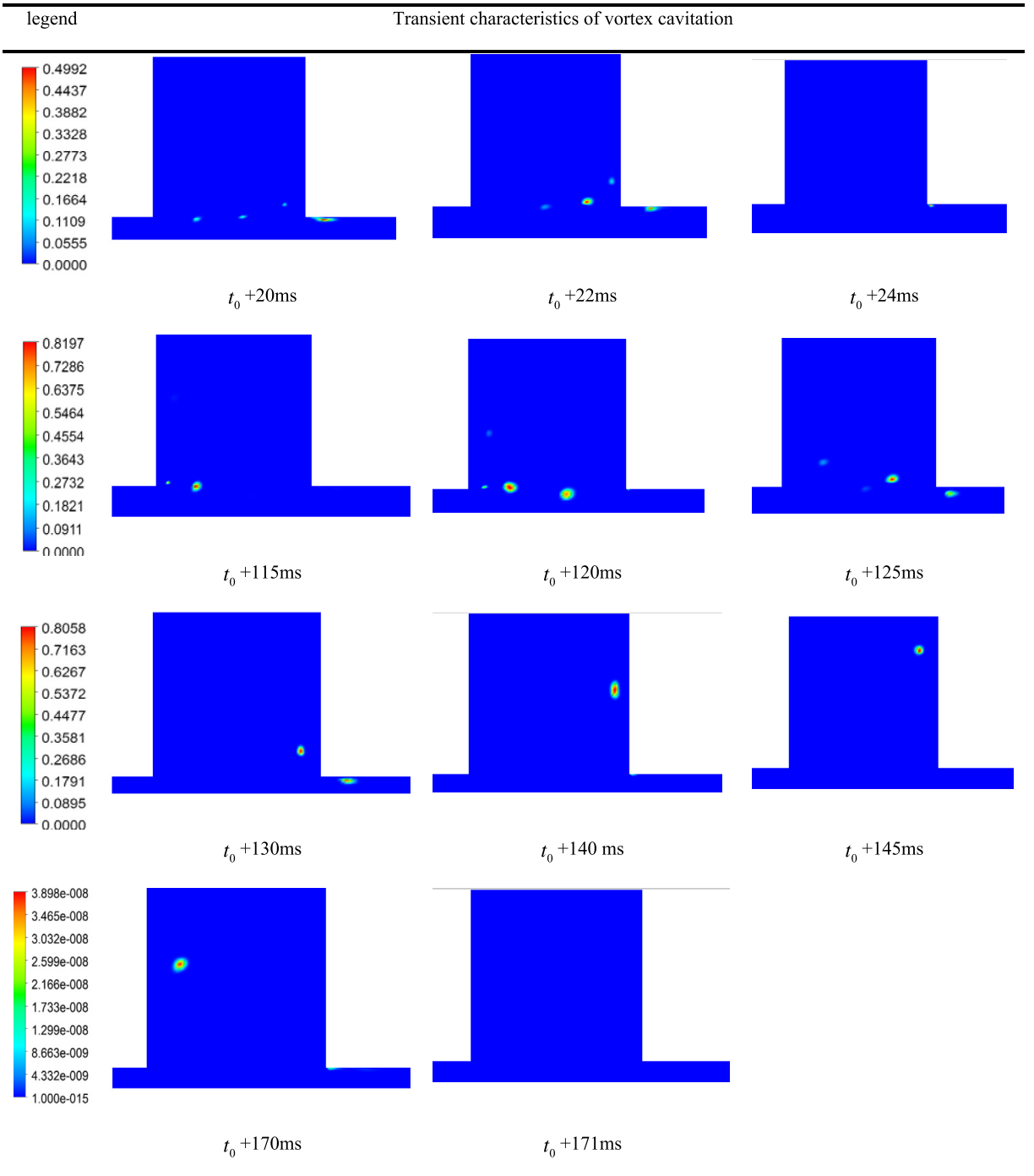

Fig. 12. Time evolution of cavitation vortices ($\sigma = 0.816,\ \mathrm{Re} = 9.96 \times 10^5$).

distribution at the shear layer. At the incipient cavitation stage, when $t = t_0 + 20$ ms, small vortices-bubbles occur at local vortices region of the shear layer. At subsequent times, from $t_0 + 20$ ms to 24 ms, the bubbles grow and move downstream, while the pressure gradients at the attachment region at trailing edge increase and their region of influence expands (see Fig. 12). At time $t = t_0 + 24$ ms, the vortex-bubbles move to the trailing edge where they encounter increasing pressure levels that eventually lead to their collapse. At $t_0 + 115$ ms, flow separation at the leading edge induces periodic vortex shedding again, and a series of new oval vortex-bubbles is generated. At $t_0 + 120$ ms. Thereafter, the vortex-bubbles are stretched and move with shear layer oscillation. At $t_0 + 125$ ms, due to increasing local pressure, bubbles with smaller vorticity collapse again whereas bubbles with high vorticity are pushed into attachment region due to oscillation of the shear layer and in the process enter into the inner cavity. In this process, the shape of the bubbles can be either spherical or oval depending on changes in the surrounding pressure. Due to screening effect, the vortex bubbles avoid the minimum pressure point during their motion as is apparent in Figs. 11 and 12. At $t_0 + 171$ ms, the pressure of the surrounding flow region increases, leading to the sudden contraction and collapse of the vortex bubbles (see Figs. 12 and 13). In the absence of detailed experimental observations, the trends described above, while qualitative in nature, serve to highlight the complexity of vortex-induced cavitation.

4.3. Wall pressure and shear layer oscillation

The predicted wall static pressure distributions on the cavity walls are plotted in Figs. 14 and 15 at several cavitations number intervals. It can be seen in Fig. 14 that the pressure fluctuates widely depending on location. Thus, for example,

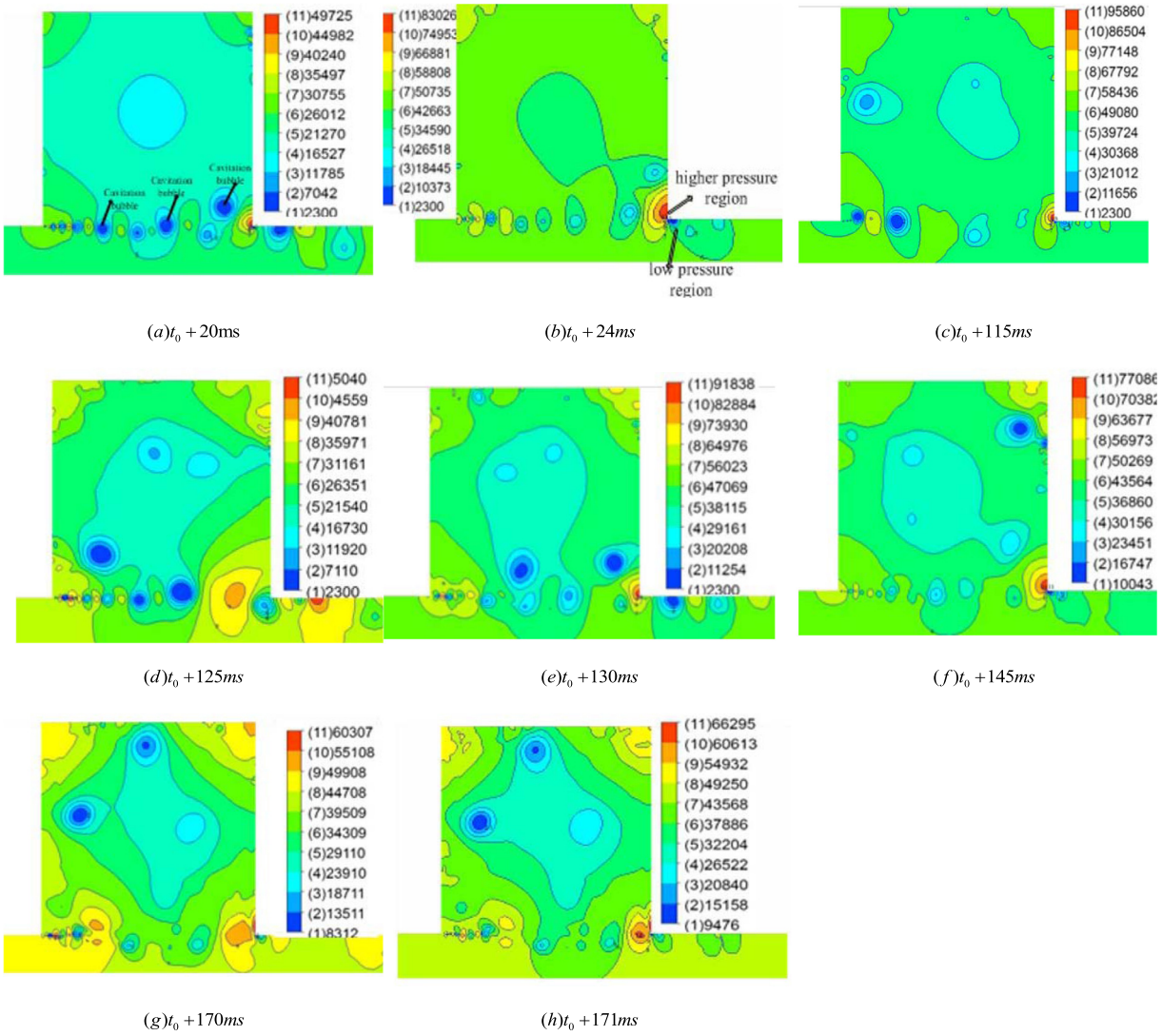

$(a)t_0 + 20\text{ms}$ $(b)t_0 + 24ms$ $(c)t_0 + 115ms$

$(d)t_0 + 125ms$ $(e)t_0 + 130ms$ $(f)t_0 + 145ms$

$(g)t_0 + 170ms$ $(h)t_0 + 171ms$

Fig. 13. Time evolution of absolute pressure in cavitation flow ($\text{Re} = 9.96 \times 10^5$).

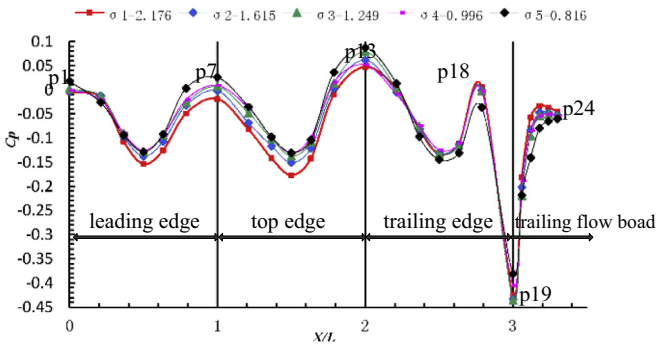

Fig. 14. Predicted variation of mean wall pressure with cavitation number.

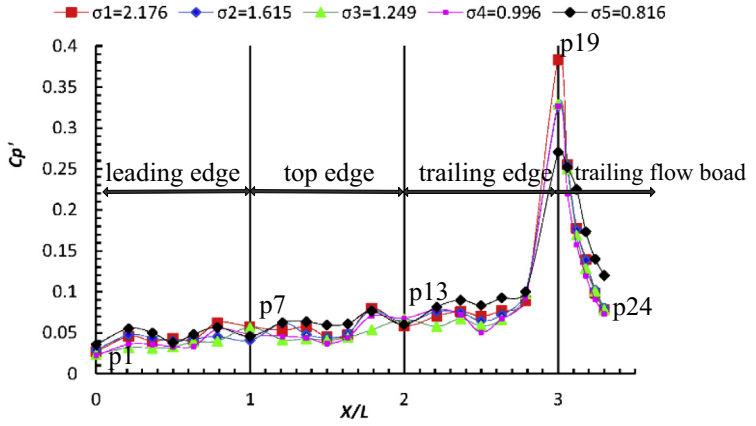

Fig. 15. Predicted variation of fluctuating wall pressure with cavitation number.

the value of the wall pressure coefficient Cp increases with decreasing σ. At $X/L = 0, 1, 2$ (which corresponds to the corner points), the Cp values show a local maximum, but at $X/L = 0.5, 1.5, 2.5$ (the middle point of every edge), the Cp values are at local minimum. As the bubbles move near the trailing edge and the trailing flow board (see Figs. 8 and 12), their presence causes the liquid density to drop, and the vapor volume fraction to increase with increasing incoming velocity. This causes a decrease in Cp. At $X/L = 3$, Cp drops to its minimum value and hence the traveling cavitation is generated here.

Fig. 15 shows the predicted distribution of the fluctuating pressure on the wall. It is clear that Cp' reaches its maximum level at the corner of trailing edge where the influence of traveling cavitation is most strongly felt, and the impact of the shear layer oscillations is quite intense. Moreover, Cp' decreases with decreasing value of σ. Thus the lower the value of σ, the more severe is the cavitation phenomena and the more is the gas content in gad-liquid mixed fluid. At $X/L \leqslant 3$, Cp' increases with increasing X/L value, but this change is very small. At $X/L > 3$, Cp' value increases with decreasing σ since this region has higher vapor content (see Fig. 16).

4.4. Frequency of vortex shedding, cavitation bubbles and shear-layer oscillation

Finally, we turn to consideration of the frequencies of the vortex shedding, and the cavitation bubble and shear-layer oscillations. The occurrence of cavitation within a cavity involves very strong coupling between the dynamics of the bubbles, the shed vortices and the shear-layer oscillations. The physical phenomenon is thus very complicated, though something of its nature can be deduced by inspection of the energy spectra of the various oscillations. It was noted earlier that the periodic collapse of traveling cavitation causes high frequency impact and results in high levels of fluctuating pressure. Fig. 17 shows the time history of the vapor volume fraction and its frequency content as obtained by performing a Fast Fourier Transform (FFT) on the signal. The locations of points 5 and 9 are shown in Fig. 8. In Fig. 18, the power spectrum of fluctuating pressure at the corner of trailing edge is shown. The high frequency at which the traveling cavitation occurs is clearly evident. Due to the influence of high frequency, the corner point at the trailing edge suffers most from the impact of the fluctuating pressure forces. Moreover, due to fluctuating pressure forces increasing as σ decreases, the strength of impact increases accordingly. It may therefore be concluded that the damage due to cavitation is likely to occur first at this location. Compared to traveling

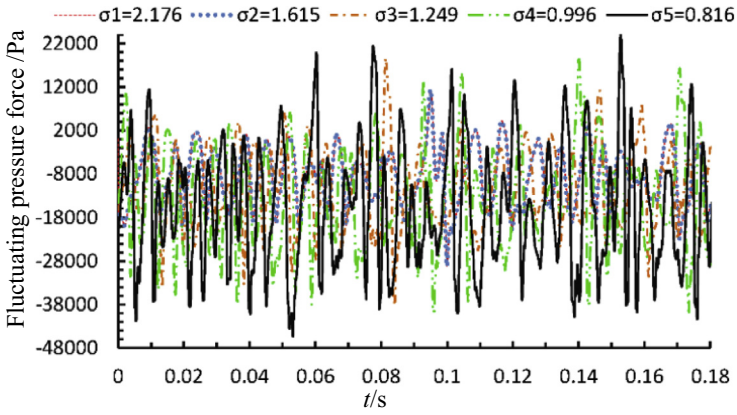

Fig. 16. Time history of fluctuating pressure at point 19 with cavitation number.

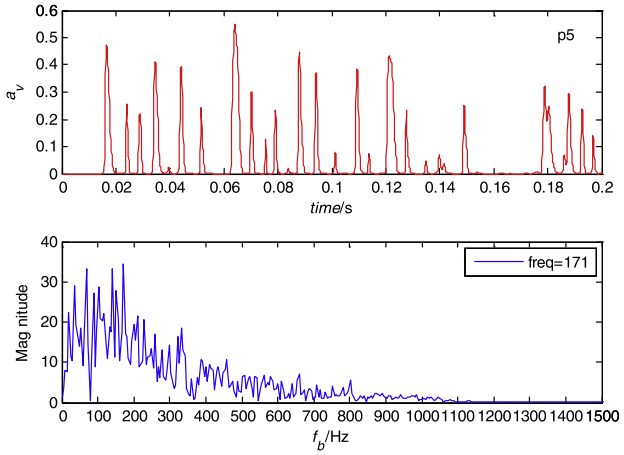

Fig. 17. FFT of vapor volume fraction at point 5 ($\sigma = 0.816,\ \mathrm{Re} = 9.96 \times 10^5$).

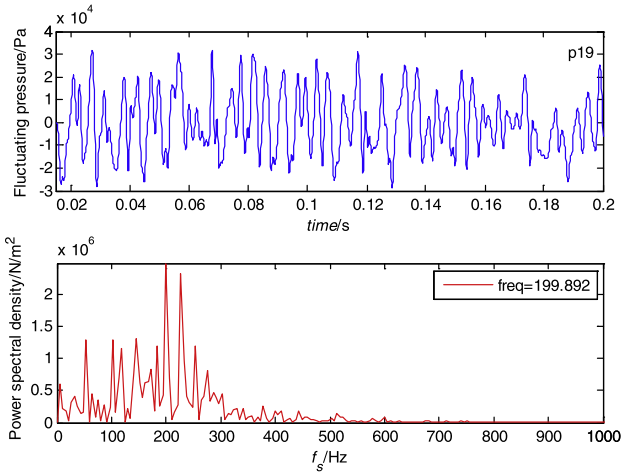

Fig. 18. Power spectral density of fluctuating pressure ($\sigma = 0.816,\ \mathrm{Re} = 9.96 \times 10^5$).

cavitation, the generation and collapse of vortex-cavitation at the shear layer is far more random in nature. Also evident in this figure is the very close coupling between the oscillations of the vortices, the bubbles and the shear layer.

Fig. 19 shows the time history of the vapor volume fraction and its associated FFT at different positions within the flow. The time history of the vortex velocity and the FFT for different cavitation numbers are shown in Fig. 20. The collapse of the vortex bubbles at the shear layer occurs at high frequency, while the bubbles moving along the fluid have low frequency characteristics. Fig. 19(a) shows that the vortex bubbles instantly collapse during their motion and thus erupt at high frequency. A small portion of the bubbles migrates into the positive pressure gradient region, thereafter vortex bubbles enter into the inner cavity along the wall and into counterclockwise rotation (see Fig. 12), while they encounter negative gradient region they may instantly collapse during motion. The frequency of bubbles motion before their collapse is the same as that of vortices (see Figs. 19(b) and 20(b)), and is about 19.5 Hz. Comparison of Fig. 20(a) and (b) shows that the frequency of vortex motion increases with decreasing value of σ. This indicates that the frequency of the vortex bubbles will increase. It can be seen that the location near the sharp corner of trailing edge has more vapor than the upstream separation zone near the leading edge. Although these two types of cavitation will erupt at high frequency, the frequency of the vortex-bubbles collapse is somewhat higher than that of the traveling cavitation at the same value of σ. A similar conclusion can be drawn from comparison of Figs. 17 and 19(a). It can be seen from the complex frequency spectra that the overall flow is characterized by three distinct frequencies, those of the bubbles and vortex motions being relatively low relative to that of the bubbles' collapse. The dominant frequency, however, is that of the shear-layer oscillations.

Fig. 22 shows the power spectrum of the fluctuating pressure at the cavity's trailing edge which is where the most intense shear-layer oscillations occur. When the cavitation number is large, several peaks appear in the power spectrum. The first of these is the frequency of the vortex-bubbles motion which at 10.5 Hz. This is nearly coincident with the frequency of the shed vortices of 10.9 Hz (Fig. 20(a)). The second is the first-order frequency of the shear-layer oscillations. The third peak value is the second-order frequency of shear-layer oscillations. These oscillations obviously strengthen with decreasing cavitation number. Moreover, the first-order frequency of oscillation dominates over the energy with increasing cavitation

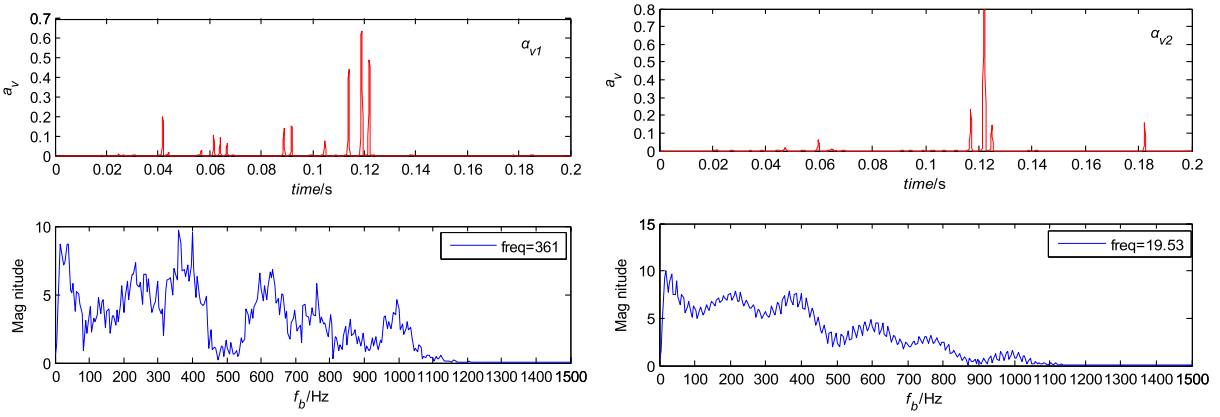

(a) FFT of α_{v1} (b) FFT of α_{v2}

Fig. 19. Time history of vapor volume fraction and FFT ($\sigma = 0.816,\ \mathrm{Re} = 9.96 \times 10^5$).

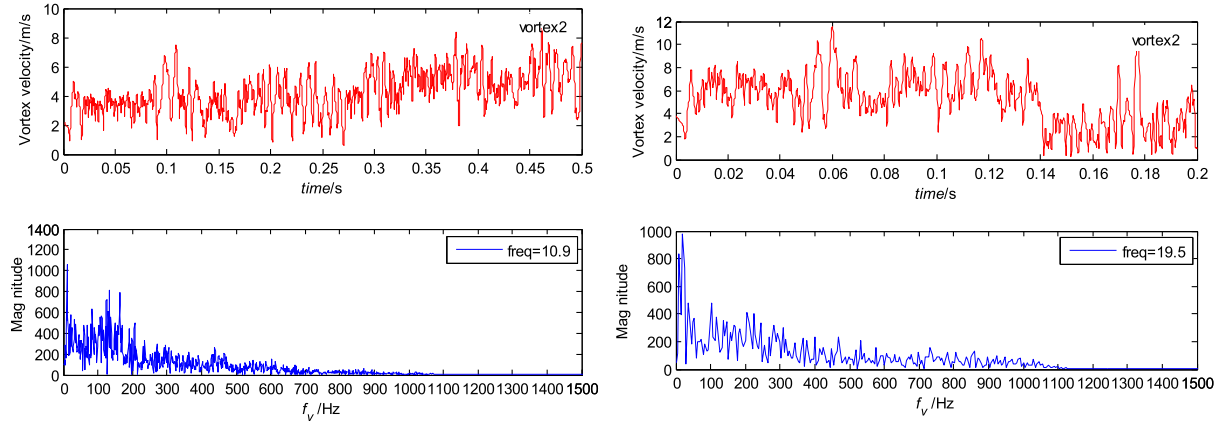

(a) $\sigma = 2.176$ (b) $\sigma = 0.816$

Fig. 20. Time history of vortex velocity and FFT.

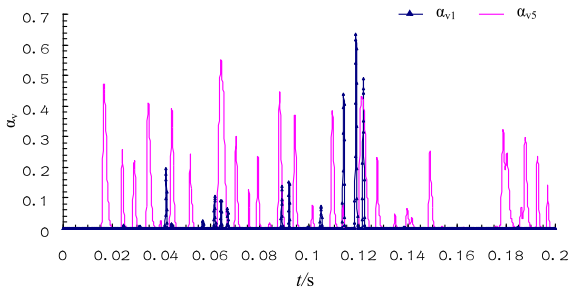

Fig. 21. Comparison of vapor volume fraction for traveling cavitation and vortex cavitation ($\sigma = 0.816,\ \mathrm{Re} = 9.96 \times 10^5$).

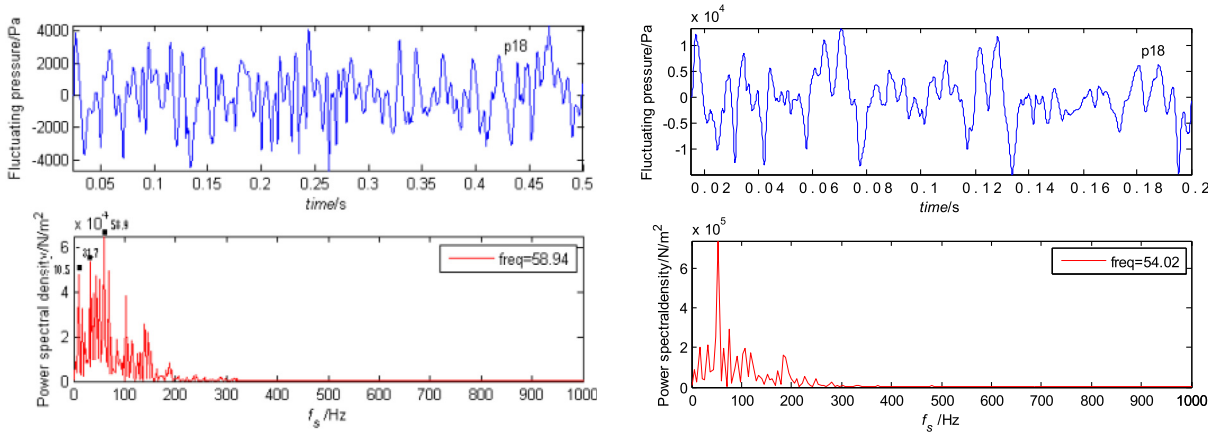

(a) $\sigma = 2.176$ (b) $\sigma = 0.816$

Fig. 22. Power spectral density of fluctuating pressure for different cavitation number.

number (see Fig. 21(b)). The conclusion that can be drawn here is that the collapse frequency of bubbles is greater than the frequency of shear-layer oscillations, whereas the frequency of the vortex motion is the lowest amongst the three.

5. Conclusions

This paper describes the development of a computational model for the prediction of cavitation induced by high-speed flow over a square surface cavity. The model is based on approach that combines Large-Eddy Simulations with the Kutoba model for the initiation and growth of the cavitation bubbles. A Volume of Fluids algorithm was used to track the oscillations of the shear layer that develops from the upstream corner. The complete model was first validated against the benchmark flows of flow over a hydrofoil at incidence where cavitation did occur, and flow within a square cavity in the absence of cavitation. In both cases, the results obtained where in general accord with data and with other computations. For the case of cavitation due to shear-layer oscillations, the predictions revealed the presence of two types of cavitation: a traveling cavitation, wherein the vapor bubbles were generated at the corner of the trailing edge, and vortex-induced cavitation generated by the shear-layer oscillations. The bubbles formed as traveling cavitation moved near the wall and most collapsed a short distance after their inception. However, a few were observed to migrate into the cavity and form a region of counter-clockwise motion below the oscillating shear layer and eventually collapsed upon encountering the region of elevated static pressure. Among the other findings of this work was the observation that the location of the point of minimum pressure coincided with the corner of trailing edge which is also where the maximum pressure fluctuations occurred. It was also observed from the computations that the mean wall static pressure decreases with increasing cavitation number, while the fluctuating pressures increase due to the influence of the traveling cavitation and the shear-layer oscillations. It was also observed that the collapse of the cavitation bubbles results in an impact frequency that is higher than the dominant frequency of the shear-layer oscillations, while the frequency of the bubbles and of the shed vortices is distinctly lower.

Acknowledgments

We gratefully acknowledge the support provided by the National Natural Science Foundation of China (Grant No. 11002038), and the Natural Science foundation of the Heilongjiang Province of China (Grant No. E201207). We also thank Professors Guoyu Wang and Inanc Senocak for providing us with experimental data for model validation.

Appendix A. Supplementary data

Supplementary data associated with this article can be found, in the online version, at http://dx.doi.org/10.1016/j.apm.2014.04.059.

References

[1] B. Huang, G.Y. Wang, B. Zhang, S.G. Shi, Assessment of cavitation models for computation of unsteady cavitating flows, J. Ship Mech. 15 (11) (2011) 1196–1201.
[2] X. Li, Y.S. Wang, C.J. Liu, Cavitation simulation of 2D hydrofoil based on homogeneous multi-phase model, J. Ship Sci. Technol. 31 (3) (2009) 31–138.
[3] S. Barre, J. Rolland, E. Goncalves, R.F. Patella, Experiments and modeling of cavitating flows in venturi: attached sheet cavitation, Eur. J. Mech. B/Fluids 28 (2009) 444–464.
[4] O. Coutier-Delgosha, R. Fortes-Patella, J.L. Reboud, N. Hakimi, C. Hirsch, Numerical simulation of cavitating flow in 2D and 3D inducer geometrie, Int. J. Numer. Methods Fluids 48 (2005) 35–167.
[5] B. Huang, G.Y. Wang, Application of DES based on k–ω SST turbulence model in computation of cavitation flows, J. China Mech. Eng. 21 (1) (2010) 85–89.
[6] N.X. Lu, R.E. Benson, G. Bark, LES of unsteady cavitation on the delft twisted foil, J. Hydrodyn. 22 (5) (2010) 784–791.
[7] E. Shams, S.V. Apte, Prediction of small scale cavitation in a high speed flow over an open cavity using large-eddy simulation, J. Fluid Eng. 132 (11) (2010) 1113011–11130114.
[8] F. Yang, Z.W. Cheng, Research progress of cavitating flow, J. Fluid Mach. 37 (11) (2009) 36–43.
[9] F. Nicond, F. Ducros, Subgrid-scale stress modeling based on the square of the velocity gradient tensor, J. Flow Turbul. Combust. 62 (3) (1999) 183–200.
[10] G. Comte-Bellot, S. Corrsin, Simple Eulerian time correlation of full and narrow band velocity signals in grid generated 'isotropic' turbulence, J. Fluid Mech. 48 (2) (1971) 273–337.
[11] F. Bakir, R. Rey, A.G. Gerber, T. Belamri, B. Hutchinson, Numerical and experimental investigations of the cavitation behavior of an inducer, J. Rotating Mach. 10 (1) (2004) 15–25.
[12] A. Kubota, H. Kato, Unsteady structure measurement of cloud cavitation on a foil section using conditional sampling techniques, J. Fluids Eng. 11 (2) (1989) 204–210.
[13] Y. Shen, P. Dimotaks, The influence of surface cavitation on hydrodynamic force, in: Proc. 22nd ATTC, St. Hohns, 1989, pp. 44–53.
[14] A.G. Gerber, A CFD Model for devices operating under extensive cavitation conditions, in: IMECE, New Orleans, Nov. 17–22, 2002, p. 39315.
[15] G.Y. Wang, I. Senocak, W. Shyy, T. Ikohagi, S.L. Cao, Dynamics of attached turbulent cavitating flows, Prog. Aerosp. Sci. 37 (2001) 551–581.
[16] B. Zhang, G.Y. Wang, B. Huang, Z.Y. Xu, Numerical and experimental studies on unsteady shedding mechanisms of cloud cavitation, J. Theor. Appl. Mech. 41 (5) (2009) 651–659.
[17] B. Huang, G.Y. Wang, Evaluation of the cavitation models on the numerical simulation of cloud cavitations, Trans. Beijing Inst. Technol. 29 (9) (2009) 786–789.
[18] H. Yamamoto, H.N. Seki, S. Fukusako, Forced-convection heat transfer on heated bottom surface of a cavity, J. Heat Transfer 101 (3) (2004) 475–479.
[19] P.K. Chang, Separation of Flow, Pergamon Press, Oxford, 1970. p. 770.
[20] S.S. Dai, X.L. Yao, Experimental research on fluid induced oscillation of 3D cave-in cavities in uniform shear layers, J. Harbin Eng. Univ. 6 (2010) 693–700.